Journal of Materials Science: Materials in Engineering

ORIGINAL PAPER Open Access

Influence of Cr on the quaternary FeTaTiW medium entropy alloy

R. Martins[1*], B. Monteiro[1], A. P. Gonçalves[2], J. B. Correia[3], A. Galatanu[4], E. Alves[1], E. Tejado[5], J. Y. Pastor[5] and M. Dias[1]

Abstract

The search for advanced materials has been growing, and high entropy alloys (HEAs) are emerging as promising candidates for application in the fusion domain. This work investigates the effect of Cr on the FeTaTiW medium entropy alloy to form $(CrFeTaTi)_{70}W_{30}$ high entropy alloy, comparing the experimental production and characterization with the simulation (molecular dynamics and hybrid molecular dynamics-Monte Carlo) of the phases formed. The alloys were produced by mechanical alloying and sintered by spark plasma sintering. Both simulations have shown that a body-centered cubic structure is formed for both compositions. Monte Carlo simulation provides a more precise prediction of microstructural formation and element segregation. Microstructural examination of the consolidated material revealed the presence of a W-rich phase and a Ti–rich phase, consistent with the phase separation observed in the MC simulations. Moreover, X-ray diffraction analysis of the milled powder for FeTaTiW and $(CrFeTaTi)_{70}W_{30}$ confirmed the formation of a bcc (body-centered cubic)-type structure with a low fraction of intermetallic phases. Mechanical testing showed ductile behavior at 1000 °C where $(CrFeTaTi)_{70}W_{30}$ showed a stress magnitude almost double that of FeTaTiW. Additionally, the thermal diffusivity between 20 and 1000 °C of both alloys increases as the temperature rises. $(CrFeTaTi)_{70}W_{30}$ exhibits an increase from 3 to 5 mm^2/s, while FeTaTiW increases from 4 to 9 mm^2/s. Still, both system's thermal diffusivity values are lower than those of CuCrZr and pure tungsten. Despite this, the study underscores the promising attributes of HEAs and highlights areas for further optimization to enhance its suitability for extreme conditions.

Keywords High entropy alloys, Molecular dynamics simulation, Hybrid molecular dynamic Monte Carlo, Thermal properties, Mechanical properties

Introduction

In recent years, significant research has been put into developing materials to enhance and optimize energy production processes. Nuclear fusion energy stands out as a promising source of energy production, relying on materials capable of withstanding demanding operational conditions with structural reliability. Extensive testing and studies have been devoted to identifying suitable materials for use in nuclear reactor divertors, with current consensus pointing towards tungsten (W) as the plasma-facing component and CuCrZr as the heat sink material (Barabash, et al. 2007). Key properties are required for a material to serve as the plasma-facing unit, for example, a high melting point, low sputter yield, and

*Correspondence:
R. Martins
ricardo.martins@ctn.tecnico.ulisboa.pt
[1] Instituto de Plasmas e Fusão Nuclear, Instituto Superior Técnico, Universidade de Lisboa, Av. Rovisco Pais, Lisboa 1049-001, Portugal
[2] C2TN, Instituto Superior Técnico, Universidade de Lisboa, Campus Tecnológico e Nuclear, Estrada Nacional 10, Bobadela LRS 2695-066, Portugal
[3] LNEG (Laboratório Nacional de Energia e Geologia), Estrada do Paço do Lumiar, Lisboa 1649-038, Portugal
[4] National Institute of Materials Physics, Magurele 077125, Romania
[5] Departamento de Ciencia de Materiales—CIME, ETSI Caminos, Canales y Puertos, Universidad Politecnica de Madrid, Madrid, Spain

minimal tritium retention (Baluc et al. Oct. 2007). Meanwhile, the heat sink material should be resistant to irradiation (Barrett et al. 2015), and the service temperature should be relatively low (Stork et al. 2014). However, the properties of the existing material do not achieve the desired operating temperatures (Stork et al. 2014). Consequently, an intermediate layer is necessary to ensure these conditions while facilitating proper thermal and mechanical properties between the materials and maintaining suitable working temperatures.

In response, the development of novel materials like high entropy alloys (HEAs) has gained attraction. Characterized by their multi-elemental composition (typically containing five or more elements), HEAs can form simple structures such as body-centered cubic (bcc) (Nong et al. 2018), face-centered cubic (fcc) (Sathiaraj et al. 2016), and hexagonal closed-packed (hcp)-type structures (Gao, et al. 1959) exhibiting exceptional properties. Moreover, HEAs have a lower relative Gibbs-free energy and a higher stability of solid solutions (Cantor et al. 2004; Yusenko et al. 2017), exhibiting a superior combination of physical and mechanical properties (Mukarram et al. 2021). HEAs offer remarkable features across various fields, including nuclear fusion, where depending on the elemental choice they exhibit significant property enhancements such as mechanical strength, even at elevated temperatures, and exceptional thermal stability as evidenced in nickel-based alloys such as (CrMnFeCoNi) (Orhan et al. 2022). Furthermore, these materials can be used to enhance other properties by changing elements such as Cr or Al on alloys such as $AlCoCr_xFeNi_{2.1}$ (Jiang et al. 2021) and $Al_{0.3}CoCrFeMnNi$ (Pohan et al. 2018), improving structural stability as shown in TiCoCrFeMn (Górniewicz et al. 2023), or enhancing the corrosion resistance in alloys such as AlCoCuFeNi-(Cr, Ti) by exploring the impact of addition of Cr or/and Ti as on it (Xiao et al. 2017).

With the fast development of HEAs, a great theoretical background and simulation, like molecular dynamics (MD), are being increasingly used for HEAs (Choi et al. 2018). Other simulation methods like the Monte Carlo (MC) method, which involves randomly swapping atom positions to achieve a more stable overall configuration, or hybrid MD-MC, which combines molecular dynamics and Monte Carlo, have been used for simulating HEAs (Widom et al. 2014) during the last years. The LAMMPS software can perform MD and MC simulations and simulate X-ray diffraction patterns based on atomistic simulation results ((Plimpton 1995; Coleman et al. Jul. 2013)). The interaction between atoms can be described using an embedded atom method (EAM) potential, which assumes that the energy of a solid is a function of the electron density. The EAM potential correlates well with more precise bonding methods and can be used for metals (Xie et al. 2013; Jelinek, et al. 2012; Sharma et al. 2016).

The objective of this work is to investigate the influence of Cr in the FeTaTiW medium entropy alloy based on computer simulation and experimental studies. Therefore, scanning electron microscopy (SEM) and X-ray diffraction (XRD) were used to perform the structural characterization of the FeTaTiW and $(CrFeTaTi)_{70}W_{30}$ alloys together with the mechanical and thermal properties of both systems.

Experimental details

The FeTaTiW and $(CrFeTaTi)_{70}W_{30}$ systems were simulated using periodic boundary conditions. The software LAMMPS developed by Sandia Labs was used for (a) molecular dynamics and (b) hybrid molecular dynamic/Monte Carlo simulations. The body-centered cubic (bcc) structure was assumed for the simulations (133 cells) with 4394 atoms. This work utilized an isothermal-isobaric (NPT) ensemble with a time step of 1 fs, while the pressure was maintained at 1 atm. The typical simulation sequence involved several steps of energy minimization of the initial configuration, heating to the simulation temperature, and energy minimization for a period of 6×10^6 time steps. The hybrid molecular dynamic/Monte Carlo simulation, hereafter referred to as MC, consisted of the introduction of a Monte Carlo swap attempt every 10 molecular dynamic simulation steps (*MC* 10:1). The embedded atom method (EAM) potentials for FeTaTiW and $(CrFeTaTi)_{70}W_{30}$ were retrieved from NIST (NIST xxxx) referring to the original work of Zhou et al. (Zhou et al. 2004). The same procedure, using the same data set for the simulation of multicomponent alloys, has already been reported in the literature (NIST xxxx). As the EAM set potential used (Zhou et al. 2004) does not include chromium, a hybrid potential (force field) was developed (Jacobson and Thompson 2022) in which the interactions involving chromium were described by the Mie potential with the parameters published in Jacobson and Thompson (2022).

The Fe, Ti, Ta, Cr, and W powders (from Alfa Aesar, 99.9% with a nominal purity and average particle size of 10 μm) were mixed in equiatomic FeTaTiW and non-equiatomic $(CrFeTaTi)_{70}W_{30}$ proportions inside a glove box. Subsequently, the powder was mechanically alloyed for 2 h at 350 rpm (rotations per minute) using a high-energy planetary ball mill, Retsch PM 400 MA, with WC balls and vials. The ball-to-powder mass ratio was 10:1. No process control agent was used. The sample and the respective atomic percentages are shown in Table 1.

The as-milled powders were then consolidated by spark-plasma sintering (SPS) on a FCT Systeme GmbH

Table 1 Atomic percentage of each element in the two samples

Designation	Cr (at.%)	Fe (at.%)	Ta (at.%)	Ti (at.%)	W (at.%)
FeTaTiW	-	25	25	25	25
$(CrFeTaTi)_{70}W_{30}$	17.5	17.5	17.5	17.5	30

sintering machine under the conditions shown in Table 2, producing a sample with a diameter of 12-mm and 3-mm thickness. After sintering, apparent density was measured using the Archimedes method (Fujii 2006).

The samples underwent metallographic preparation involving grinding with SiC paper and subsequent polishing with diamond suspensions (6 µm, 3 µm, and 1 µm). Further refinement was achieved through fine polishing using colloidal silica suspension (0.2 µm).

Microstructural analysis was performed using secondary electrons (SE) and backscattered electrons (BSE) with a JEOL JSM-7001F field emission gun (SEM), equipped with an Oxford EDS spectrometer. Powder X-ray diffraction (PXRD) was used to investigate the evolution of the powder mixtures using a Philips X'Pert diffractometer in a Bragg–Brentano geometry with Cu K_α radiation, over a 2θ range from 10 to 80° with a step size of 0.03°. The consolidated samples were analyzed using a Bruker-AXS D8 diffractometer geometry with Cu K_α radiation, over a 2θ range from 10 to 80° with a step size of 0.01°. The simulation of the phases was performed used the PowderCell software (Kraus and Nolze 1996).

Three-point bending (TPB) tests were performed on a Sigmatest Materialprüftechnik GmbH, Wedel, Germany, coupled to an Instron 8501 universal electromechanical testing machine (Instron, High Wycombe, UK) with alumina bars for bending/compression testing. The heating rate was 10 °C/min, held for 10 min for the thermal stabilization of the system before testing. The (1.0×1.1×11 mm) sample was tested using a loading span of 10 mm and 100 µm/min crosshead speed under a high vacuum atmosphere (1×10^{-6} mBar) at 25 °C, 600 °C, and 1000 °C.

Thermal diffusivity was performed on LFA 427 equipment with an InSb sensor with 600 V and a pulse width of 0.5 ms from 20 to 1000 °C under a vacuum atmosphere.

Table 2 SPS conditions for each composition and apparent density calculated by Archimedes method

Sample	Temperature (°C)	Load (kN)	Holding time (min)	Apparent density (%)
FeTaTiW	1100	9	5	93
$(CrFeTaTi)_{70}W_{30}$	1100	9	5	92

Thermodynamics calculations were first performed to determine the possible structures formed in the alloys and to help through the interpretation and discussion of the results. Based on empirical models (Guo and Liu 2011; Zhang et al. 2008) using the enthalpies and entropies of mixing, ΔH_{mix} and ΔS_{mix}, the fractional atomic size differences δ, and the valence electron concentrations (VEC), it is possible to predict the formation of solid solutions. In this context, calculations of the relevant properties of FeTaTiW and $(CrFeTaTi)_{70}W_{30}$ alloys are presented in Table 3. Based on the calculated values (Guo and Liu 2011), the existence of a bcc solid solution is expected for both FeTaTiW and $(CrFeTaTi)_{70}W_{30}$ compositions. The choice of a non-equiatomic composition for the alloy with Cr ($(CrFeTaTi)_{70}W_{30}$) is related to the fact that according to theoretical calculations, the equiatomic CrFeTaTiW does not form a solid solution since the atomic size difference factor is lower than 6.5. Therefore, a different composition for the chromium alloy was selected.

Results and discussion

Simulation

Simulations involving molecular dynamic (MD) and hybrid molecular dynamic/Monte Carlo (MC) were performed similarly to previous research already published (Dias et al. 2023; F. of M. P. with N. C. H. E. A. 2022) for FeTaTiW and $(CrFeTaTi)_{70}W_{30}$ alloys. It is important to note that interstitial impurities such as WC, O, and C, which may arise from mechanical alloying and SPS sintering, were not included in the simulation. Figure 1a and b shows the FeTaTiW and $(CrFeTaTi)_{70}W_{30}$ alloy potential energy (Ep) and chemical segregation as a function of temperature, respectively. Both systems display analogous potential energy (Ep) performance for MD and MC simulations. MC simulation always yielded the lowest values of potential energy for both compositions up to 2250 °C, corresponding to a more stable structure. The MC potential energy converges to the values observed on MD simulation at higher temperatures, especially for the FeTaTiW system. On the other hand, the chemical

Table 3 Thermodynamic calculations for FeTaTiW and $(CrFeTaTi)_{70}W_{30}$ alloys

	FeTaTiW	$(CrFeTaTi)_{70}W_{30}$
ΔHmix	−11 kJ/mol	−8.2 kJ/mol
ΔS_{mix}	11.53 J/(K.mol) Medium entropy alloy	13.4 J/(K.mol) High entropy alloy
δ	6.13	6.2
VEC	5.75	5.8
Structure predicted	bcc	bcc

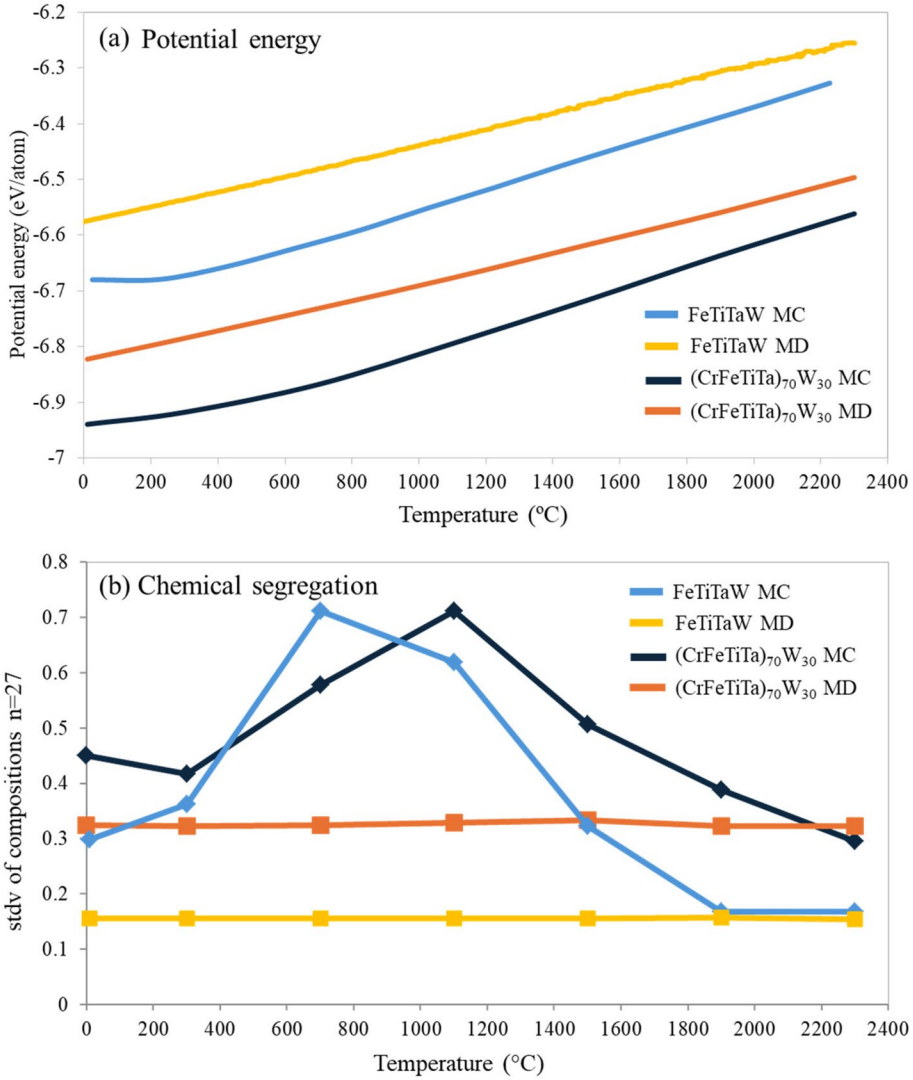

Fig. 1 MD and MC simulations showing the **a** potential energy versus temperature and **b** chemical segregation vs temperature for FeTaTiW and $(CrFeTaTi)_{70}W_{30}$ systems

segregation simulation results indicate similar behaviors. The MD simulations yield a small standard deviation, approximately constant with temperature, reflecting the random distribution of the elements. In contrast, the MC simulation showed a much higher degree of segregation, increasing with temperature, until 700 °C for FeTaTiW and 1100 °C for $(CrFeTaTi)_{70}W_{30}$, followed by a decrease in segregation with increasing temperatures, reaching similar values to those of the MD simulation. An analogous chemical segregation procedure was used in (Dias et al. 2023; Martins, et al. 2024), i.e., chemical analysis in 27 locations within the simulation cell to reflect the dispersion of chemical compositions.

The simulation of crystal structure for FeTaTiW and $(CrFeTaTi)_{70}W_{30}$ entropy alloys for MD and MC at 25 °C, 427 °C, and 1627 °C is shown in Figs. 2 and 3, respectively. At low and intermediate temperatures (25 °C and 427 °C), Ti and W segregation are observed for both FeTaTiW simulations. Above 1800 °C, the segregation is undetectable, and a similar structure is predicted above this temperature with both MC and MD simulation, consisting of a single-phase solid solution, i.e., medium entropy alloy. The lattice parameters derived from the FeTaTiW simulation cells were 0.31 nm for MC and 0.31 nm for MD at 25 °C. The densities extracted from the simulations at 25 °C were 12.49 g/cm^3 for MC and 12.43 g/cm^3 for MD.

The $(CrFeTaTi)_{70}W_{30}$ simulations shown in Fig. 3 evidence some W segregation. The MC simulation shows titanium segregation at low and intermediate temperatures (25 °C and 427 °C), and at 1627 °C, a comparable

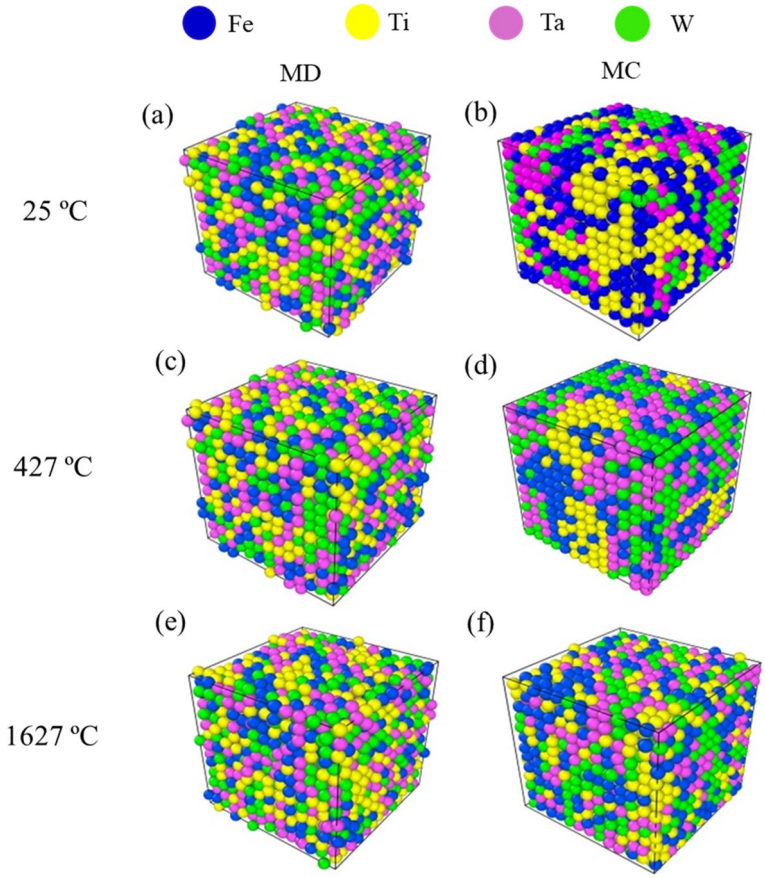

Fig. 2 Simulation results for MD and MC structures for FeTaTiW at **a** and **b** 25 °C, **c** and **d** 427 °C, and **e** and **f** 1627 °C, respectively

structure is predicted with both the MC and MD simulations, corresponding to a single-phase solid solution, i.e., a high entropy alloy. The lattice parameters derived from the $(CrFeTaTi)_{70}W_{30}$ simulation cells were 0.31 nm for MC and 0.31 nm for MD at 25 °C. The densities extracted from the simulations at 25 °C were 13.22 g/cm^3 for MC and 13.14 g/cm^3 for MD.

Figure 4 shows the pair distribution function for FeTaTiW and $(CrFeTaTi)_{70}W_{30}$ alloys. In addition, Fig. 4 supports previous simulation results, where at low and intermediate temperatures the pair distribution function determines that Ti and W segregation can occur as displayed by the MC simulation (very high probability of a W–W and Ti–Ti bond, see the arrow in the magnification of Fig. 4a and b). Moreover, in Fig. 4c, $(CrFeTaTi)_{70}W_{30}$ MC simulations show that at low and intermediate temperatures, Ti segregation results from very high probability of Ti–Ti bond. However, the FeTaTiW system shows a lower probability of a Ti–Ti bond when compared to $(CrFeTaTi)_{70}W_{30}$, where the highest probability of a Ti–Ti bond occurs at 823 °C. Above 2023 °C major Ti, W segregations are undetectable, and a similar structure is predicted with both MC and MD simulation, consisting of a single-phase solid solution. In both the MC and MD types of simulation, the crystal structure obtained was a bcc-type structure.

X-ray diffraction

Figure 5 shows the X-ray diffraction of (a) FeTaTiW and (b) $(CrFeTaTi)_{70}W_{30}$ for the mixture of pure elements, milled powder, and consolidated materials. After 2 h of milling, the individual peaks of the elements disappeared, and a bcc-type structure was formed with a lattice parameter of 0.32 nm for FeTaTiW and 0.32 nm for $(CrFeTaTi)_{70}W_{30}$. The formation of a bcc-type structure for both compositions is in agreement with the thermodynamic calculations, and the simulation is shown in the "Simulation" section. Furthermore, WC peaks were also observed after 2 h of milling for both samples, which is related to contamination from the WC container and vials. Additionally, the same figure shows the diffractograms of the consolidated samples of FeTaTiW and $(CrFeTaTi)_{70}W_{30}$. Each diffractogram exhibits a major bcc-type structure with a lattice parameter of 0.32 nm

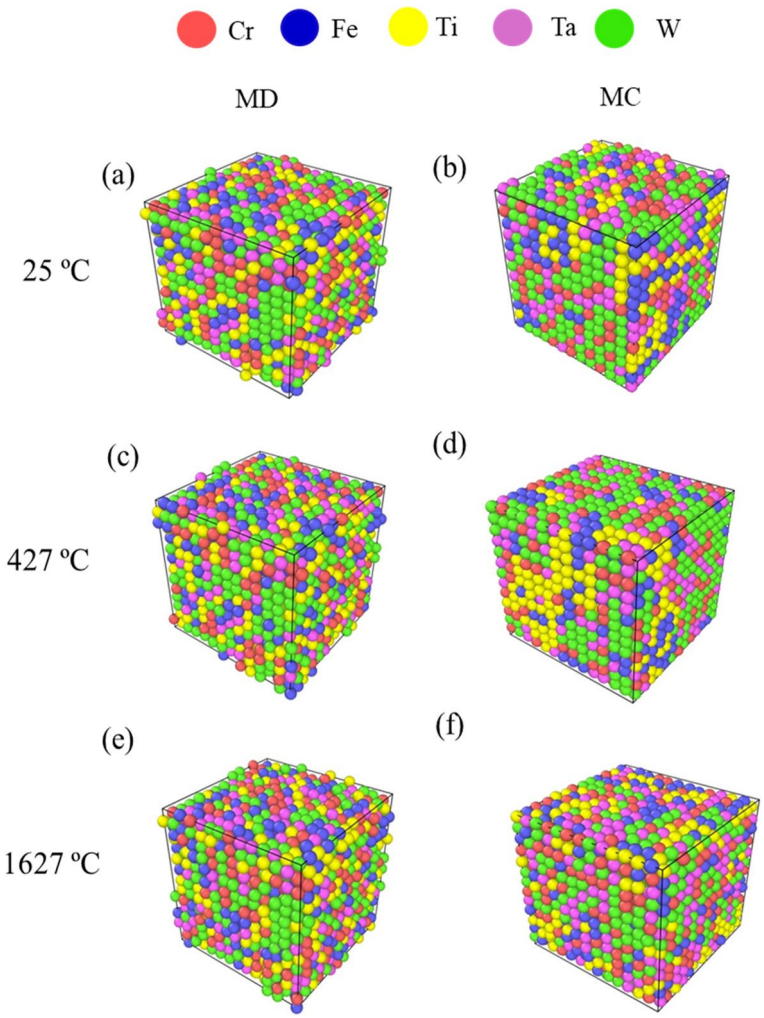

Fig. 3 Simulation results for MD and MC structures for $(CrFeTaTi)_{70}W_{30}$ at **a** and **b** 25 °C, **c** and **d** 427 °C and **e** and **f** 1627 °C, respectively

for FeTaTiW together with the presence of an intermetallic phase (rhombohedral crystal structure (space group 166) (Kraus and Nolze 1996) indicated by the triangles in Fig. 5a3. In addition, in the experimental X-ray of the FeTaTiW, there are small peaks of a non-identified structure (indicated by black spots). The intermetallic phase adopts a type structure as A_7B_6, in which five distinct Wyckoff atomic positions: 3a, 6c′, 6c″, 6c‴ and 18 h (Gasper et al. 2024) can be observed. The 3a site has a coordination number of 12 and can accommodate either A-type or B-type atoms, and the 6c′, 6c″, and 6c‴ positions, with the coordination numbers 15, 16, and 14, respectively, are generally filled by A-type atoms from groups 5 or 6 of the periodic table. Finally, the 18-h position, characterized by a coordination number of 12, is typically occupied by smaller B-type atoms such as Fe, Co, Ni, and Zn. This combination results in the stoichiometric compositions of the μ phase: A_7B_6 or A_6B_7 (Gasper et al. 2024; Ostrowska and Cacciamani 2020; Joubert and Dupin 2004). The peaks observed in Fig. 5a3 on the consolidated material are similar to those associated with the μ phases displayed by several studies (Joubert and Dupin 2004; Alloys 2022). The formation of the μ phase is common in various binary and ternary systems, especially in multicomponent alloys such as high entropy alloys. These alloys typically include A-type refractory elements, such as Mo, Ta, and W, alongside B-type late transition elements like Fe, Co, and Ni (Ostrowska and Cacciamani 2020).

The diffractogram of the $(CrFeTaTi)_{70}W_{30}$ displays a bcc-type structure similar to FeTaTiW, with a lattice parameter of 0.32 nm together with the presence of another intermetallic/nonstoichiometric phases (rhombohedral crystal structure (space group 194) indicated by the squares in Fig. 5b3) (Kraus and Nolze 1996). This intermetallic phase is similar to a CrTiFe ternary

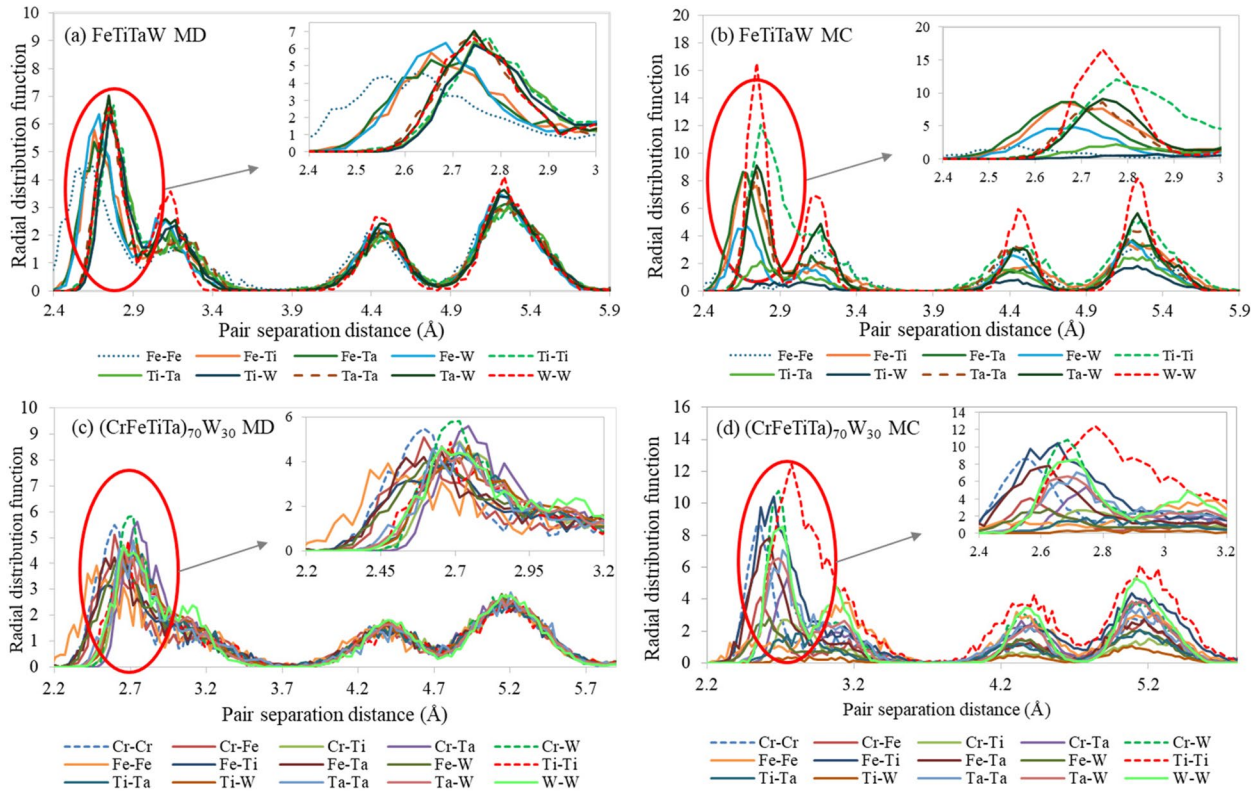

Fig. 4 Simulation pair distribution function results at 25 °C for **a** MD and **b** MC FeTaTiW simulation and for **c** MD and **d** MC $(CrFeTaTi)_{70}W_{30}$ system

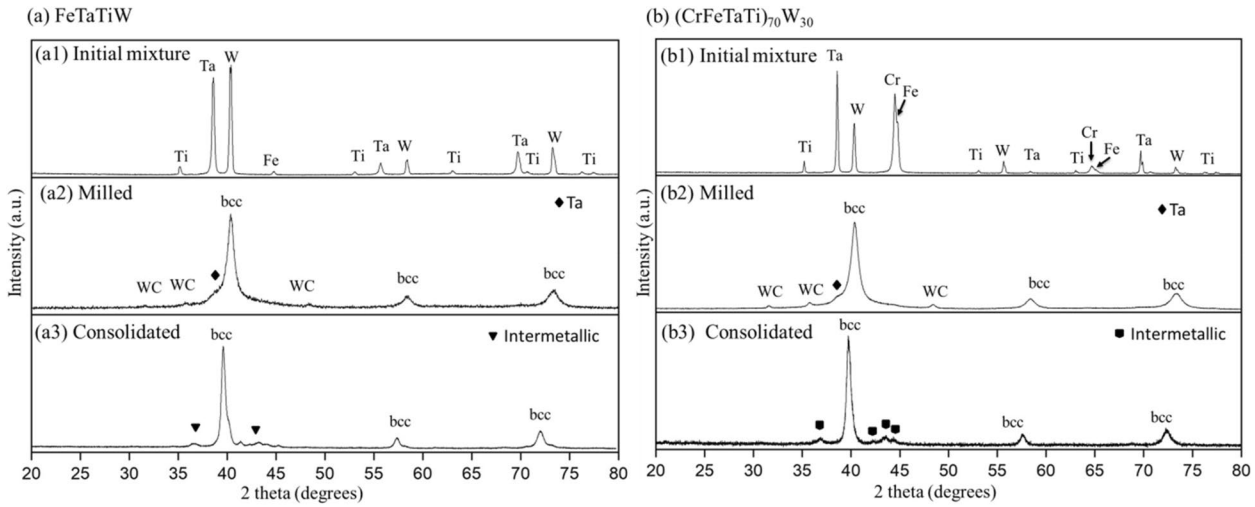

Fig. 5 X-ray diffraction of **a** FeTaTiW for the a1 mixture of pure elements, a2 milled powder, and a3 consolidated sample. X-ray diffraction of **b** $(CrFeTaTi)_{70}W_{30}$ for the b1 the mixture of pure elements, b2 milled powder, and b3 consolidated one

phase. The Ti–Fe binary diagram presents two intermetallic compounds: TiFe (B2-type structure) and $TiFe_2$ (C14-type structure, Laves phase) (Bo, et al. 2012). The introduction of an alloying element (M) results in the formation of a ternary MTiFe alloy with a general AB_2-type structure. When Cr is present along with Fe and Ti, the CrTiFe ternary phase alloy can be established, as was observed in several studies (Bo, et al. 2012; Wang et al. 2016; Ivanchenko and Pryadko xxxx) and in

agreement with the ternary phase diagram (Ivanchenko and Pryadko xxxx).

Microstructure analysis

Figure 6 shows the morphology of the milled powder and consolidated samples for (a) FeTaTiW and (b) $(CrFeTaTi)_{70}W_{30}$, respectively. The images revealed that the powders milled for both samples consisted of small particles agglomerated with homogeneous elements dispersion, corroborating with the diffractograms shown in Fig. 5 a2 and b2 milled powder. Moreover, the consolidated microstructures for FeTaTiW and $(CrFeTaTi)_{70}W_{30}$ are exhibited in Fig. 6a2 and b2, respectively. Both samples show fine microstructures with small dark-phase regions.

The EDS maps are shown in the same figures to identify the distribution of the elements in each phase. For the case of FeTaTiW, it is possible to distinguish W-rich regions (indicated by the red arrow in Fig. 6a2) together with Ti–rich phases (dark regions indicated by the white arrow in Fig. 6a2) surrounded by Fe-rich phase (indicated by the yellow arrow in Fig. 6a2). This Fe-rich region and the homogeneously distributed tantalum may explain the Fe_6Ta_7 phase seen in the experimental diffractograms. On the other hand, the EDS for $(CrFeTaTi)_{70}W_{30}$ revealed the presence of W-rich regions (bright region indicated by the red arrow in Fig. 6b2) and Ti–rich regions (dark region indicated by the withe arrow in Fig. 6b2). Figure 6b2 shows another region (indicated by a yellow arrow), corresponding to the Fe- and Cr-rich area, as exhibited in Fig. 6 b4 and b5, respectively, and a major phase with all the elements, but with less Ti and W amounts. Therefore, the results of the microstructure observations seem to be in agreement with the experimental diffractograms and with the MC simulation exhibited in Figs. 1, 4, and5.

Mechanical properties

Figure 7 illustrates the flexural stress–strain curves for the consolidated medium and high entropy alloys: (a) FeTaTiW and (b) $(CrFeTaTi)_{70}W_{30}$, tested at temperatures of 25 °C, 600 °C, and 1000 °C. At 25 °C and 600 °C, both alloys exhibit a brittle behavior, characterized by a sharp increase in stress followed by fracture with a maximum stress of 830 MPa for FeTaTiW measured at 600 °C. However, at 1000 °C, both alloys display a ductile behavior. In particular, the FeTaTiW alloy demonstrates higher flexural stress values in the brittle state when compared to the $(CrFeTaTi)_{70}W_{30}$ alloy. On the other hand, in the ductile state displayed at 1000 °C, FeTaTiW shows a stress magnitude of almost half when compared with $(CrFeTaTi)_{70}W_{30}$. This indicates that FeTaTiW has a

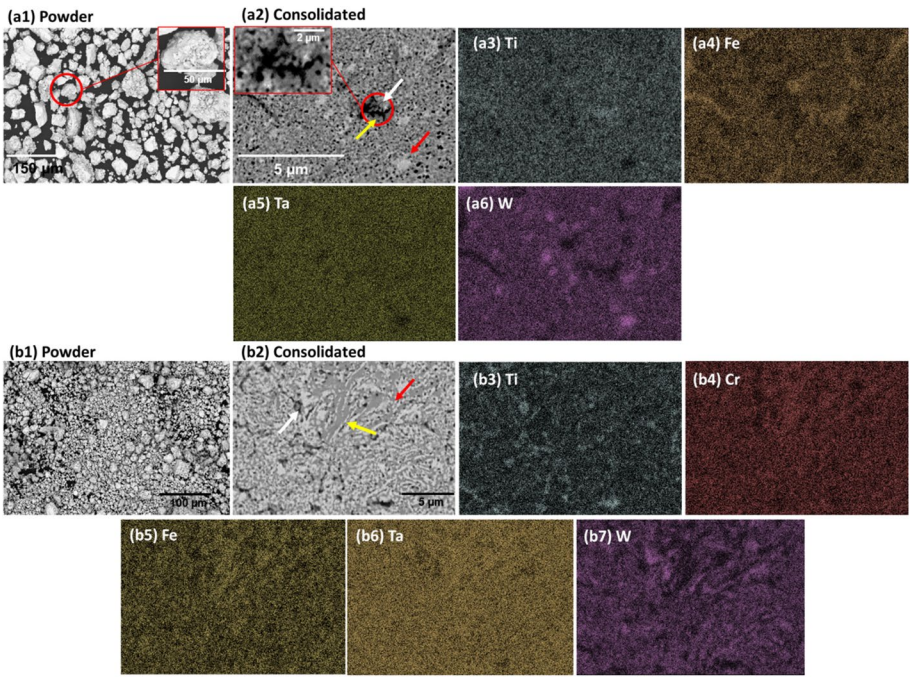

Fig. 6 SEM images for **a** FeTaTiW system and **b** $(CrFeTaTi)_{70}W_{30}$ system. SEM image a1 milled FeTaTiW powder, a2 consolidated FeTaTiW sample, a3 EDS for Ti, a4 EDS for Fe, a5 EDS for Ta, a6 EDS for W maps. SEM images of the b1 milled $(CrFeTaTi)_{70}W_{30}$) powder and b2 consolidated $(CrFeTaTi)_{70}W_{30}$ samples, b3 EDS for Ti, b4 EDS for Cr, b5 EDS for Fe, b6 EDS for Ta, and b7 EDS for W maps. X-ray lines for a3 and b3 Ti-Kα, b4 Cr-Kα, a4 and b5 Fe-Lα, a5 and b6 Ta-Lα, and a6 and b7 W-Lα

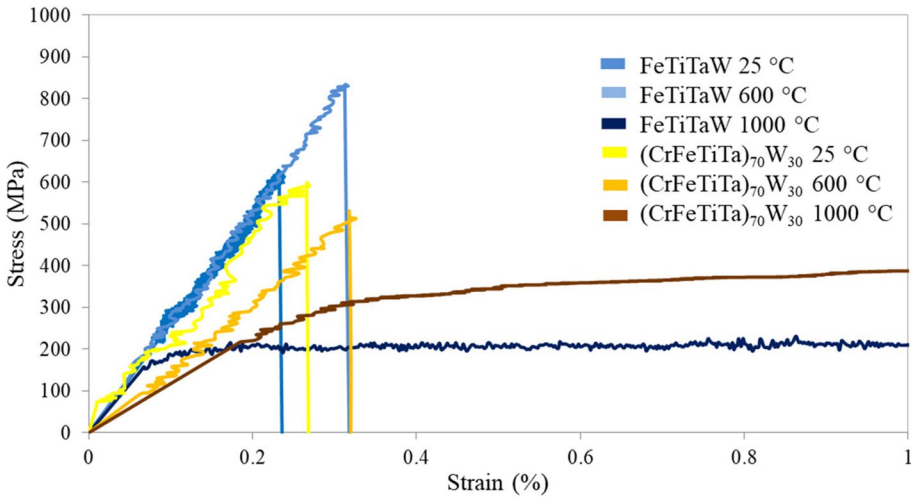

Fig. 7 Stress–strain flexural curves as a function of temperature for consolidated FeTaTiW and $(CrFeTaTi)_{70}W_{30}$ high entropy alloys at 25 °C, 600 °C, and 1000 °C

higher resistance to fracture at lower temperatures. However, the stress magnitude values at elevated temperatures are lower when compared to $(CrFeTaTi)_{70}W_{30}$.

In the 3-point bending tests displayed in Fig. 8, the FeTaTiW alloys show an increase in flexural strength from 496 to 607 Mpa, achieving its maximum value at 600 °C, followed by a decrease to 286 Mpa exhibited at 1000 °C. The $(CrFeTaTi)_{70}W_{30}$ alloy exhibits a constant flexural strength from 25 to 600 °°C, followed by a decrease in flexural strength from 507 to 378 MPa, exhibited at 1000 °C. Remarkably, at 1000 °C, the flexural strength exhibited by the $(CrFeTaTi)_{70}W_{30}$ alloy is considerably higher than the FeTaTiW alloy.

Notably, the flexural strengths of both FeTaTiW and $(CrFeTaTi)_{70}W_{30}$ surpass those of high-entropy alloys developed previously for the same application (F. of M. P. with N. C. H. E. A. 2022) and appear to have similar values of flexural stress when compared to FeTaTiVW (Martins, et al. 2024) and even higher than CrNbTaVW (F. of M. P. with N. C. H. E. A. 2022) and $CrNbTaVW_{1.7}$ (F.

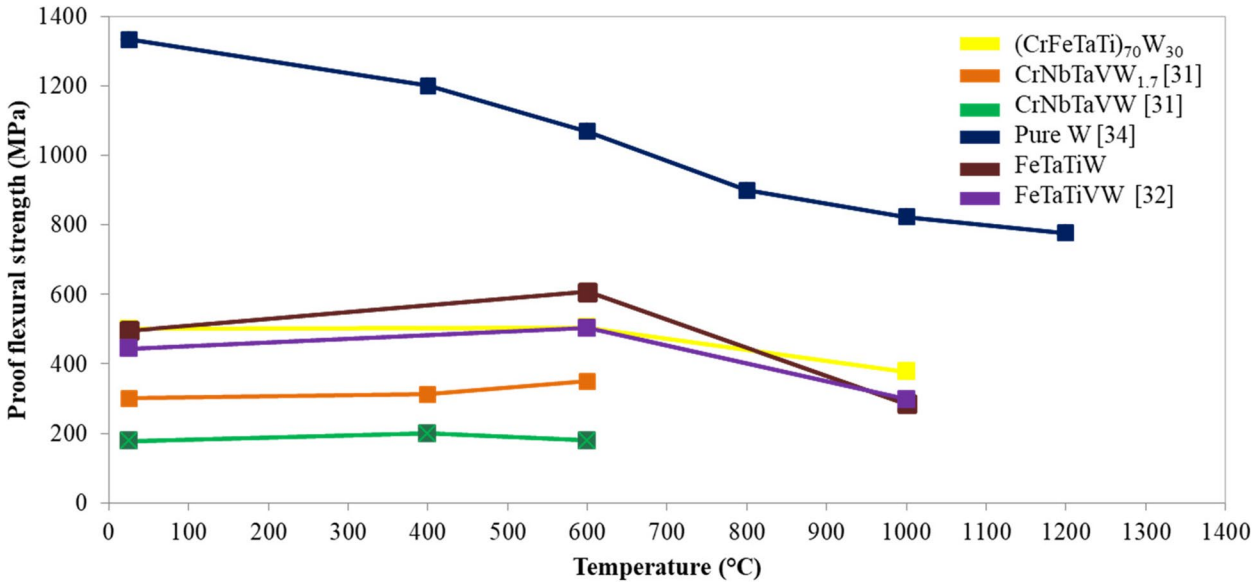

Fig. 8 Proof flexural strength as a function of temperature of the alloys $(CrFeTaTi)_{70}W_{30}$, FeTaTiW presented in this work together with CrNbTaVW, $CrNbTaVW_{1.7}$, FeTiTaVW, and Plansee rolled W for comparison

of M. P. with N. C. H. E. A. 2022) ones. All systems mentioned above appear to be in the range of those reported for other RHEAs by Senkov et al. (Senkov et al. 2018), shown in Fig. 9 for compression testing.

The fracture surfaces of the samples tested at 25 °C and 600 °C for FeTaTiW and $(CrFeTaTi)_{70}W_{30}$ are shown in Fig. 10. A refined nanometric microstructure (avg. grain size ~ 100 nm) can be observed for both 25 °C and 600 °C specimens, with mostly intergranular fracture, although some residual coarse W grains can be identified by their distinct cleavage characteristics (as indicated in Fig. 10a by the white arrow). However, none of these larger

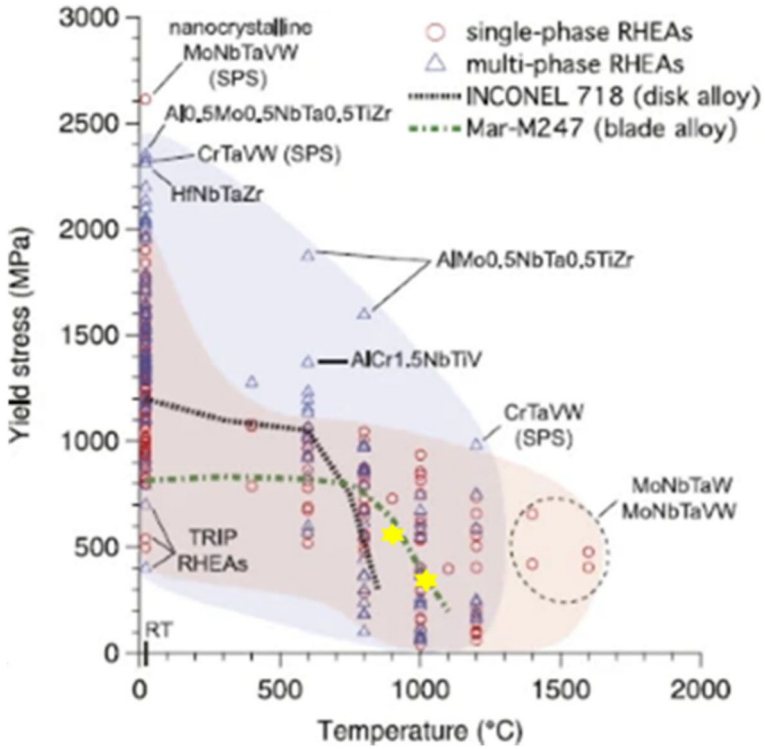

Fig. 9 Values from Senkov (Senkov et al. 2018)

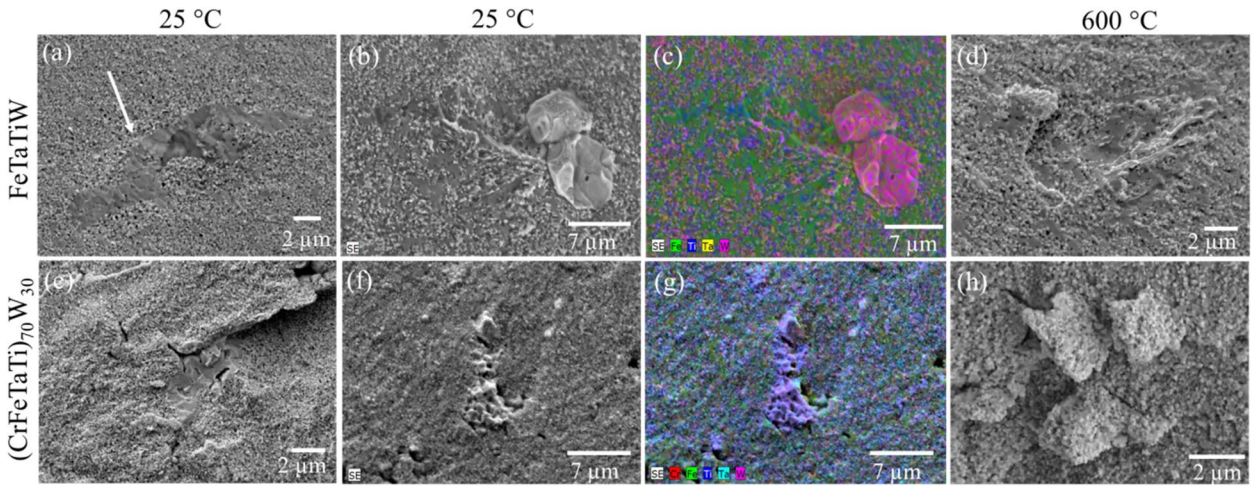

Fig. 10 Fracture surfaces of **a** and **b** FeTaTiW and **c** and **d** $(CrFeTaTi)_{70}W_{30}$ alloy tested at room temperature. EDS compositional mapping showing the **a** FeTaTiW and **b** $(CrFeTaTi)_{70}W_{30}$ with non-mixed W particles in the fracture surface of the CrFeTaTiW alloy

grains was identified as crack initiators since they mostly originated in the corners of the specimens, as these are stress concentrators. With increasing temperature, slight changes can be observed, with subtle rounding of the grains at 1000 °C. The EDS composition maps of the RT fracture surfaces assessed the presence of two phases in its microstructure: a major multielement-phase, non-mixed W particles and minor Fe-Ti–rich phases, as observed in the XRD diffractograms of the consolidated material but probably due to the lack of resolution of the EDS spot on a highly rough fracture surface, and this latter phase could not be identified by itself in our analyses.

Thermal diffusivity

The temperature-dependent behavior of thermal diffusivity for FeTaTiW and $(CrFeTaTi)_{70}W_{30}$ entropy alloys from 25 to 1000 °C is presented in Fig. 11. Both samples exhibit similar thermal diffusivity behavior as a function of temperature, with diffusivity values increasing as temperature rises. The chromium incorporation notably reduces the thermal diffusivity of $(CrFeTaTi)_{70}W_{30}$ by approximately 25% compared to FeTaTiW, a similar reduction to that observed when compared to VFeTaTiW (Martins, et al. 2024) and even larger when compared to pure tungsten (Pradère et al. 2006) and CuCrZr ((Rohde et al. 2014; Copper and "CuCr1Zr", 2024)) (see Fig. 11a), since both FeTaTiW and $(CrFeTaTi)_{70}W_{30}$ present significantly lower diffusivity values. NiCoFeCrMn and NiCoFeCrPd HEAs studies (Jin et al. 2017) provide a detailed examination of thermal diffusivity at elevated temperatures, showing values similar to those observed in FeTaTiW and $(CrFeTaTi)_{70}W_{30}$. Furthermore, research on the non-equiatomic $W_{57}Ta_{21}V_{11}Ti_8Cr_3$ alloy (Li, et al. 2022) revealed thermal diffusivity values ranging from 10 to 15 mm^2/s which also increased with temperature. In high entropy alloys, the phonon mean free path is short due to the atomic-level disorder, leading to high phonon scattering rates. As proposed by the author in Lu et al. (2013), the enhanced thermal diffusivity observed at higher temperatures in HEAs is attributed to lattice dilation, which lengthens the phonon mean free path as the temperature increases. Consequently, this is a critical characteristic for the design of HEAs for specific thermal applications.

Conclusion

This work presents a structural and thermal characterization together with an insight into the simulation to better understand the microstructure and properties that the addition of an element (chromium) has on a medium entropy alloy (FeTaTiW). Simulation is a crucial instrument for high entropy alloy phase prediction, which can be an extremely vital tool to improve these new materials and produce the most accurate results possible.

The Monte Carlo simulations reveal a more stable structure by displaying lower Gibbs free energies for FeTaTiW and $(CrFeTaTi)_{70}W_{30}$ alloy systems and revealed to be more accurate by predicting a substantial degree of segregation with increasing temperature when compared with molecular dynamics. Both the FeTaTiW and $(CrFeTaTi)_{70}W_{30}$ pair distribution functions show a very high probability of a Ti–Ti bond. However, there is a lower probability of a Ti–Ti bond on $(CrFeTaTi)_{70}W_{30}$ when compared to FeTaTiW. This segregation suggested by the MC simulation was corroborated by microstructural analysis, highlighting the presence of Ti–rich and W-rich phases.

The mechanical study of both alloys indicates a ductile behavior at 1000 °C while at 25 °C and 600 °C

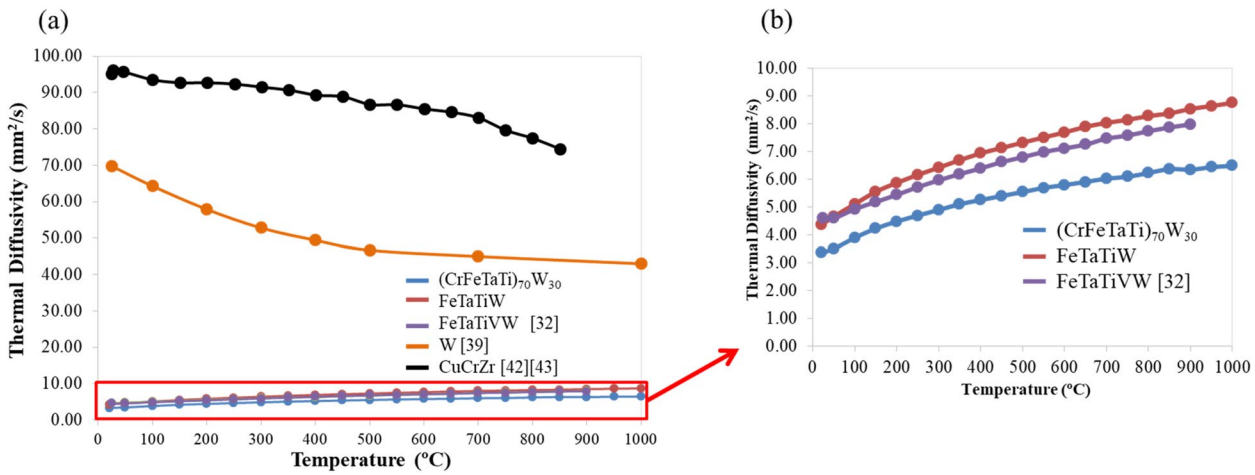

Fig. 11 **a** Thermal diffusivity for the FeTaTiW and $(CrFeTaTi)_{70}W_{30}$ consolidated sample and for FeTaTiVW, pure W and CuCrZr. **b** Magnification of FeTaTiW and $(CrFeTaTi)_{70}W_{30}$ and FeTaTiVW systems

evidences a brittle one, implying a ductile to brittle transition temperature above this temperature. The flexural strength data from the 3-point bending tests demonstrates an increase in strength with rising temperatures up to 600 °C followed by a reduction in strength at 1000 °C. In particular, the flexural strengths of both FeTaTiW and $(CrFeTaTi)_{70}W_{30}$ surpass those of many other high-entropy alloys reported in the literature.

The thermal diffusivity of the FeTaTiW and $(CrFeTaTi)_{70}W_{30}$ alloys showed a slight increase with temperature, attributed to lattice dilation, which lengthens the phonon mean free path as temperature rises. It was observed that chromium incorporation reduces the thermal diffusivity by approximately 25% compared to FeTaTiW, although values remained in the range of 3 to 9 mm^2/s far below those of CuCrZr and W. Nevertheless, both entropy alloy systems displayed comparable results with other similar RHEAs, always been lower than 15 (mm^2/s).

These findings show that the addition of chromium to FeTaTiW to form $(CrFeTaTi)_{70}W_{30}$ HEA significantly changes both the mechanical and thermal properties. More studies are required, not only to evaluate other compositions to improve the mechanical properties and understand the role each element plays but also to evaluate irradiation damage in the future, a key factor for their development as fusion-relevant materials.

Acknowledgements
Not applicable.

Authors' contributions
RM, conceptualization, data curation, investigation, formal analysis, and writing — original draft. BM, investigation and data curation. APG, resources and validation. JBC, formal analysis, software, resources, and methodology. AG, resources, methodology, and data curation. EA, supervision and funding acquisition. ET, investigation, formal analysis, and validation. JYP, investigation, formal analysis, and validation. MD, supervision, conceptualization, project administration conception, formal analysis, and funding acquisition.

Funding
IPFN activities were supported by FCT — Fundação para a Ciência e Tecnologia, I.P., by project reference UIDB/50010/2020 and DOI identifierhttps://doi.org/10.54499/UIDB/50010/2020(https://doi.org/10.54499/UIDB/50010/2020), by project reference UIDP/50010/2020 and DOI identifier DOIhttps://doi.org/10.54499/UIDP/50010/2020(https://doi.org/10.54499/UIDP/50010/2020), and by project reference LA/P/0061/2020 and DOIhttps://doi.org/10.54499/LA/P/0061/2020(https://doi.org/10.54499/LA/P/0061/2020). This work has been carried out within the framework of the EUROfusion Consortium, funded by the European Union via the Euratom Research and Training Programme (Grant Agreement No. 101052200 — EUROfusion). Views and opinions expressed are however those of the author(s) only and do not necessarily reflect those of the European Union or the European Commission. Neither the European Union nor the European Commission can be held responsible for them.

Data Availability
Not applicable.

Declarations

Competing interests
The authors declare the following financial interests/personal relationships which may be considered as potential competing interests: Marta Dias reports financial support which was provided by the Instituto Superior Técnico, Universidade de Lisboa. Marta Dias reports a relationship with Instituto Superior Técnico that includes employment. The other authors declare that they have no competing interests.

Received: 7 January 2025 Accepted: 9 March 2025
Published online: 09 April 2025

References

Liu, T. W., Li, T., & Dai, L. H. 2022 Near-Equiatomic μ Phase in Self-Sharpening Tungsten-Based High-Entropy Alloys. Metals 12(7). https://doi.org/10.3390/met12071130

N Baluc Oct. 2007 Status of R&D activities on materials for fusion power reactors Nucl Fusion 47 10 S696 S717 https://doi.org/10.1088/0029-5515/47/10/S18

V. Barabash *et al.*, "Materials challenges for ITER - current status and future activities," *J. Nucl. Mater.*, vol. 367–370 A, no. SPEC. ISS., pp. 21–32, 2007, https://doi.org/10.1016/j.jnucmat.2007.03.017.

TR Barrett 2015 Enhancing the DEMO divertor target by interlayer engineering Fusion Eng des 98–99 1216 1220 https://doi.org/10.1016/j.fusengdes.2015.03.031

H. Bo *et al.*, "Thermodynamic re-assessment of Fe-Ti binary system," *Trans. Nonferrous Met. Soc. China (English Ed.*, vol. 22, no. 9, pp. 2204–2211, 2012, https://doi.org/10.1016/S1003-6326(11)61450-7.

B. Cantor, I. T. H. Chang, P. Knight, and A. J. B. Vincent, "Microstructural development in equiatomic multicomponent alloys," *Mater. Sci. Eng. A*, vol. 375–377, no. 1–2 SPEC. ISS., pp. 213–218, 2004, https://doi.org/10.1016/j.msea.2003.10.257.

WM Choi YH Jo SS Sohn S Lee BJ Lee 2018 "Understanding the physical metallurgy of the CoCrFeMnNi high-entropy alloy: an atomistic simulation study", *npj Comput* Mater 4 1 1 9 https://doi.org/10.1038/s41524-017-0060-9

SP Coleman DE Spearot L Capolungo Jul. 2013 Virtual diffraction analysis of Ni [0 1 0] symmetric tilt grain boundaries Model Simul Mater Sci Eng 21 5 055020https://doi.org/10.1088/0965-0393/21/5/055020

F. M. Copper, "CuCr1Zr," 2024.

M. Dias, P. A. Carvalho, A. P. Gonçalves, E. Alves, and J. B. Correia, "Intermetallics Hybrid molecular dynamic Monte Carlo simulation and experimental production of a multi-component Cu – Fe – Ni – Mo – W alloy," *Intermetallics*, vol. 161, no. May, p. 107960, 2023, https://doi.org/10.1016/j.intermet.2023.107960.

F. of M. P. with N. C. H. E. A. Antão *et al.*, "Improvement of mechanical properties with non-equimolar CrNbTaVW high entropy alloy," *Crystals*, vol. 12, no. 2, pp. 1–10, 2022, https://doi.org/10.3390/cryst12020219.

K Fujii 2006 Precision density measurements of solid materials by hydrostatic weighing Meas Sci Technol 17 10 2551 2559 https://doi.org/10.1088/0957-0233/17/10/004

M. C. Gao *et al.*, "High-entropy alloys in hexagonal close packed structure," pp. 5–7, 1959.

C Gasper IY Gao FA Busch A Ziemons D Beckers H Springer 2024 Preparation of binary and ternary laves and l -phases in the Ta – Fe (– Al) system for property analysis at the microscale Metall Mater Trans A 55 7 2244 2263 https://doi.org/10.1007/s11661-024-07390-z

D. Górniewicz, K. Karczewski, Z. Bojar, and S. Jóźwiak, "Structural stability of titanium-based high-entropy alloys assessed based on changes in grain size and hardness," *Materials (Basel).*, vol. 16, no. 23, 2023, https://doi.org/10.3390/ma16237361.

S Guo CT Liu 2011 Phase stability in high entropy alloys: formation of solid-solution phase or amorphous phase Prog Nat Sci Mater Int 21 6 433 446 https://doi.org/10.1016/S1002-0071(12)60080-X

V. Ivanchenko and T. Pryadko, "Chromium – iron – titanium." Springer-Verlag Berlin Heidelberg. https://doi.org/10.1007/978-3-540-74199-2_17.

D. W. Jacobson and G. B. Thompson, "Revisting Lennard Jones, Morse, and N-M potentials for metals," *Comput. Mater. Sci.*, vol. 205, no. January, p. 111206, 2022, https://doi.org/10.1016/j.commatsci.2022.111206.
B. Jelinek *et al.*, "Modified embedded atom method potential for Al, Si, Mg, Cu, and Fe alloys," *Phys. Rev. B - Condens. Matter Mater. Phys.*, vol. 85, no. 24, 2012, https://doi.org/10.1103/PhysRevB.85.245102.
H. Jiang, L. Li, R. Wang, K. Han, and Q. Wang, "Effects of chromium on the microstructures and mechanical properties of AlCoCrxFeNi2.1 eutectic high entropy alloys," *Acta Metall. Sin. (English Lett.*, vol. 34, no. 11, pp. 1565–1573, 2021, https://doi.org/10.1007/s40195-021-01303-4.
K Jin 2017 Thermophysical properties of Ni-containing single-phase concentrated solid solution alloys Mater des 117 185 192 https://doi.org/10.1016/j.matdes.2016.12.079
JM Joubert N Dupin 2004 Mixed site occupancies in the μ phase Intermetallics 12 12 1373 1380 https://doi.org/10.1016/j.intermet.2004.04.036
W Kraus G Nolze 1996 Powder Cell - a program for the representation and manipulation of crystal structures and calculation of the resulting X-ray powder patterns J Appl Crystallogr 29 3 301 303 https://doi.org/10.1107/S0021889895014920
Y. Li *et al.*, "Preliminary exploration of a WTaVTiCr high-entropy alloy as a plasma-facing material," *Nucl. Fusion*, vol. 62, no. 12, 2022, https://doi.org/10.1088/1741-4326/ac8fa5.
CL Lu SY Lu JW Yeh WK Hsu 2013 Thermal expansion and enhanced heat transfer in high-entropy alloys J Appl Crystallogr 46 3 736 739 https://doi.org/10.1107/S0021889813005785
R. Martins *et al.*, "Simulation , structural , thermal and mechanical properties of the FeTiTaVW high entropy alloy," 2024.
M. Mukarram, M. A. Munir, M. Mujahid, and K. Yaqoob, "Systematic development of eutectic high entropy alloys by thermodynamic modeling and experimentation: an example of the cocrfeni-mo system," *Metals (Basel).*, vol. 11, no. 9, 2021, https://doi.org/10.3390/met11091484.
NIST, "Interatomic potentials repository." [Online]. Available: https://www.ctcms.nist.gov/potentials/
ZS Nong YN Lei JC Zhu 2018 Wear and oxidation resistances of AlCrFeNiTi-based high entropy alloys Intermetallics 101 February 144 151 https://doi.org/10.1016/j.intermet.2018.07.017
OK Orhan M Isiet L Caparini M Ponga 2022 Exploring the compositional space of high-entropy alloys for cost-effective high-temperature applications Front Mater 8 January 1 15 https://doi.org/10.3389/fmats.2021.816610
M Ostrowska G Cacciamani 2020 Thermodynamic modelling of the σ and μ phases in several ternary systems containing Co, Cr, Fe, Mo, Re and W J Alloys Compd 845 156122https://doi.org/10.1016/j.jallcom.2020.156122
S. Plimpton, "Fast parallel algorithms for short-range molecular dynamics," 1995.
RM Pohan 2018 Microstructures and mechanical properties of mechanically alloyed and spark plasma sintered Al0.3CoCrFeMnNi high entropy alloy Mater Chem Phys 210 62 70 https://doi.org/10.1016/j.matchemphys.2017.09.013
C Pradère JM Goyhénèche JC Batsale S Dilhaire R Pailler 2006 Thermal diffusivity measurements on a single fiber with microscale diameter at very high temperature Int J Therm Sci 45 5 443 451 https://doi.org/10.1016/j.ijthermalsci.2005.05.010
P. S. Productspecification, "W-sheet dimensions and tolerances thickness- and width tolerances." pp. 2–7.
M Rohde 2014 Intercomparison of thermal diffusivity measurements on CuCrZr and PMMA High Temp - High Press 42 6 469 474
GD Sathiaraj MZ Ahmed PP Bhattacharjee 2016 Microstructure and texture of heavily cold-rolled and annealed fcc equiatomic medium to high entropy alloys J Alloys Compd 664 109 119 https://doi.org/10.1016/j.jallcom.2015.12.172
Senkov ON, Miracle DB, Chaput KJ, Couzinie JP (2018) Development and exploration of refractory high entropy alloys - a review. J Mater Res 33(19):3092–3128. https://doi.org/10.1557/jmr.2018.153
A Sharma P Singh DD Johnson PK Liaw G Balasubramanian 2016 Atomistic clustering-ordering and high-strain deformation of an Al0.1 CrCoFeNi high-entropy alloy Sci Rep 6 March 1 11 https://doi.org/10.1038/srep31028
D Stork 2014 Developing structural, high-heat flux and plasma facing materials for a near-term DEMO fusion power plant: the EU assessment J Nucl Mater 455 1–3 277 291 https://doi.org/10.1016/j.jnucmat.2014.06.014
S. Wang, K. Wang, G. Chen, Z. Li, Z. Qin, and X. Lu, "CALPHAD : computer coupling of phase diagrams and thermodynamic modeling of Ti-Fe-Cr ternary system," *Calphad*, vol. 56, no. September 2016, pp. 160–168, 2017, https://doi.org/10.1016/j.calphad.2016.12.007.
M. Widom, W. P. Huhn, S. Maiti, and W. Steurer, "Hybrid molecular dynamic Monte Carlo simulation and experimental production of a multi-component Cu–Fe–Ni–Mo–W alloy/molecular dynamics simulation of a refractory metal high entropy alloy," *Metall. Mater. Trans. A Phys. Metall. Mater. Sci.*, vol. 45, no. 1, pp. 196–200, 2014, https://doi.org/10.1007/s11661-013-2000-8.
DH Xiao 2017 Microstructure, mechanical and corrosion behaviors of AlCoCuFeNi-(Cr, Ti) high entropy alloys Mater des 116 438 447 https://doi.org/10.1016/j.matdes.2016.12.036
L. Xie, P. Brault, A. L. Thomann, and J. M. Bauchire, "AlCoCrCuFeNi high entropy alloy cluster growth and annealing on silicon: a classical molecular dynamics simulation study," *Appl. Surf. Sci.*, vol. 285, no. PARTB, pp. 810–816, 2013, https://doi.org/10.1016/j.apsusc.2013.08.133.
KV Yusenko 2017 First hexagonal close packed high-entropy alloy with outstanding stability under extreme conditions and electrocatalytic activity for methanol oxidation Scr Mater 138 22 27 https://doi.org/10.1016/j.scriptamat.2017.05.022
Y Zhang YJ Zhou JP Lin GL Chen PK Liaw 2008 Solid-solution phase formation rules for multi-component alloys Adv Eng Mater 10 6 534 538 https://doi.org/10.1002/adem.200700240
X. W. Zhou, R. A. Johnson, and H. N. G. Wadley, "Misfit-energy-increasing dislocations in vapor-deposited CoFe/NiFe multilayers," *Phys. Rev. B - Condens. Matter Mater. Phys.*, vol. 69, no. 14, pp. 1–10, 2004, https://doi.org/10.1103/PhysRevB.69.144113.

Publisher's Note